

---

This is an electronic reprint of the original article.  
This reprint may differ from the original in pagination and typographic detail.

Khosravian, Maryam; Koch, Rouven; Lado, Jose

**Hamiltonian learning with real-space impurity tomography in topological moiré superconductors**

*Published in:*  
JPhys Materials

*DOI:*  
[10.1088/2515-7639/ad1c04](https://doi.org/10.1088/2515-7639/ad1c04)

Published: 18/01/2024

*Document Version*  
Publisher's PDF, also known as Version of record

*Published under the following license:*  
CC BY

*Please cite the original version:*  
Khosravian, M., Koch, R., & Lado, J. (2024). Hamiltonian learning with real-space impurity tomography in topological moiré superconductors. *JPhys Materials*, 7(1), 1-14. Article 015012 . <https://doi.org/10.1088/2515-7639/ad1c04>

---

This material is protected by copyright and other intellectual property rights, and duplication or sale of all or part of any of the repository collections is not permitted, except that material may be duplicated by you for your research use or educational purposes in electronic or print form. You must obtain permission for any other use. Electronic or print copies may not be offered, whether for sale or otherwise to anyone who is not an authorised user.

PAPER • OPEN ACCESS

## Hamiltonian learning with real-space impurity tomography in topological moiré superconductors

To cite this article: Maryam Khosravian *et al* 2024 *J. Phys. Mater.* **7** 015012

View the [article online](#) for updates and enhancements.

You may also like

- [Robust observable control of open and closed quantum systems](#)  
Vaibhav Bhutoria, Andrew Koswara and Raj Chakrabarti
- [Electron paramagnetic resonance and photochromism of  \$N\_3V^0\$  in diamond](#)  
B L Green, B G Breeze and M E Newton
- [Replica analysis of the lattice-gas restricted Boltzmann machine partition function](#)  
David C Hoyle

**PRIME**  
PACIFIC RIM MEETING  
ON ELECTROCHEMICAL  
AND SOLID STATE SCIENCE

HONOLULU, HI  
Oct 6–11, 2024

Abstract submission deadline:  
**April 12, 2024**

Learn more and submit!

**Joint Meeting of**  
The Electrochemical Society  
•  
The Electrochemical Society of Japan  
•  
Korea Electrochemical Society



## PAPER

## OPEN ACCESS

RECEIVED  
25 August 2023REVISED  
18 December 2023ACCEPTED FOR PUBLICATION  
8 January 2024PUBLISHED  
18 January 2024

Original Content from  
this work may be used  
under the terms of the  
[Creative Commons  
Attribution 4.0 licence](#).

Any further distribution  
of this work must  
maintain attribution to  
the author(s) and the title  
of the work, journal  
citation and DOI.



# Hamiltonian learning with real-space impurity tomography in topological moiré superconductors

Maryam Khosravian<sup>1,\*</sup> , Rouven Koch<sup>1</sup>  and Jose L Lado 

Department of Applied Physics, Aalto University, 02150 Espoo, Finland

<sup>1</sup> These two authors contributed equally.

\* Author to whom any correspondence should be addressed.

E-mail: [maryam.khosravian@aalto.fi](mailto:maryam.khosravian@aalto.fi)**Keywords:** topological superconductivity, machine learning, deep learning, van der Waals heterostructures, Moiré materials

## Abstract

Extracting Hamiltonian parameters from available experimental data is a challenge in quantum materials. In particular, real-space spectroscopy methods such as scanning tunneling spectroscopy allow probing electronic states with atomic resolution, yet even in those instances extracting the effective Hamiltonian is an open challenge. Here we show that impurity states in modulated systems provide a promising approach to extracting non-trivial Hamiltonian parameters of a quantum material. We show that by combining the real-space spectroscopy of different impurity locations in a moiré topological superconductor, modulations of exchange and superconducting parameters can be inferred via machine learning. We demonstrate our strategy with a physically-inspired harmonic expansion combined with a fully-connected neural network that we benchmark against a conventional convolutional architecture. We show that while both approaches allow extracting exchange modulations, only the former approach allows inferring the features of the superconducting order. Our results demonstrate the potential of machine learning methods to extract Hamiltonian parameters by real-space impurity spectroscopy as local probes of a topological state.

## 1. Introduction

Learning Hamiltonian parameters from experimental data is one of the most critical open problems in order to bring together experiments with theoretical models [1–8]. Conventionally, phenomenological models to account for experimental data are developed on a case by case basis. In certain instances, obtaining the Hamiltonian parameters of the model can be done by fitting specific features of the data [9, 10]. Many-body Hamiltonians with local interactions can be extracted local observables by exploiting time evolution and quantum Hamiltonian tomography, a strategy demonstrated theoretically and experimentally [11–16]. However, in some instances, no simple fitting procedure nor time-dependent measurements can be performed to extract Hamiltonian parameters. Machine learning methods have risen as a powerful approach to extract subtle features of data, and in particular they have become successful in tackling inverse problems in quantum materials [17–28].

Van der Waals heterostructures are a paradigmatic system in which, thanks to their tunability, a variety of quantum Hamiltonians can be emulated [29]. Specifically, the capability of combining two-dimensional materials with radically different properties allows engineering systems simultaneously hosting antagonist order [30, 31], with the paradigmatic example of van der Waals heterostructures combining 2D magnets and superconductors [32–36]. Beyond the different coexisting orders, van der Waals materials bring a unique feature to heterostructures, the emergence of a moiré pattern [37–41]. The moiré pattern stems from the structural modulation in real space due to a twist angle between lattices. Most importantly, the moiré modulation leads to a spatial modulation of all the Hamiltonian parameters. This modulation is the driving force behind a variety of phenomena, including topological and correlated states in van der Waals

heterostructures [42–54]. However, extracting the values of these modulations in moiré system is an open problem, as their effect on the electronic structure is greatly challenging to disentangle. Interestingly, the coexistence of a moiré pattern and local impurities opens up a new strategy to infer electronic parameters due to their non-trivial interplay [55–59].

In our manuscript, we put forward a method to extract Hamiltonian parameters of unconventional moiré superconductors using machine learning and impurity engineering. Specifically, we show that thanks to the moiré pattern, local impurities give rise to dramatically different electronic excitations depending on the location of the moiré pattern. This dependency allows us to directly infer moiré modulations via a machine learning algorithm that takes as input excitations for different impurity locations. We demonstrate that our algorithm allows extracting modulation strengths of exchange proximity and superconducting order, two parameters that cannot be directly extracted from a measured local density of states (LDOS). We further address the robustness of our algorithm to noise, showing that Hamiltonian parameters can be extracted in an experimentally realistic scenario.

## 2. Methods

### 2.1. Model

We consider an artificial two-dimensional superconductor obtained by combining a two-dimensional ferromagnet and a two-dimensional superconductor [32–34] as shown in figure 1(a). The electronic structure of the heterostructure is modeled with an atomistic Wannier orbital site forming a triangular lattice, where the moiré pattern is incorporated in the modulation of the Hamiltonian parameters [60–64]. The full Hamiltonian takes the form

$$\mathcal{H}_0 = \mathcal{H}_{\text{kin}} + \mathcal{H}_J + \mathcal{H}_R + \mathcal{H}_{\text{SC}} \quad (1)$$

with  $\mathcal{H}_{\text{kin}} = t \sum_{\langle ij \rangle, s} c_{i,s}^\dagger c_{j,s} + \mu \sum_i c_{i,s}^\dagger c_{i,s}$  with  $c_{n,s}^\dagger$  ( $c_{n,s}$ ) the creation (annihilation) fermionic operator with spin  $s$  in site  $n$ . The combination of exchange coupling, Rashba spin–orbit coupling and superconducting proximity gives rise to topological superconducting state when combined on the right footing [32, 65–70]. We focus on the regime giving rise to topological superconducting states  $C = 1, 2, 3$ , which arise when taking the chemical potential crossing the  $\Gamma, K, M$  points, respectively. The hopping is controlled by  $t$ , the chemical potential by  $\mu$  and  $\langle i, j \rangle$  runs over nearest neighbors. The term  $\mathcal{H}_R = i\lambda_R \sum_{\langle ij \rangle, ss'} \mathbf{d}_{ij} \cdot \sigma^{s,s'} c_{i,s}^\dagger c_{j,s'}$  is the Rashba spin–orbit coupling arising from mirror symmetry breaking at the interface [71], with  $\sigma$  the spin Pauli matrices,  $\lambda_R$  controls the spin–orbit coupling constant and  $\mathbf{d}_{ij} = (\mathbf{r}_i - \mathbf{r}_j) \times \hat{z}$ .

We now focus on the main terms that we will extract with our procedure, the modulated exchange and modulated superconductivity. The exchange coupling is included in a term

$$\mathcal{H}_J = \sum_{i,s,s'} J(\mathbf{r}) \sigma_z^{s,s'} c_{i,s}^\dagger c_{i,s'} \quad (2)$$

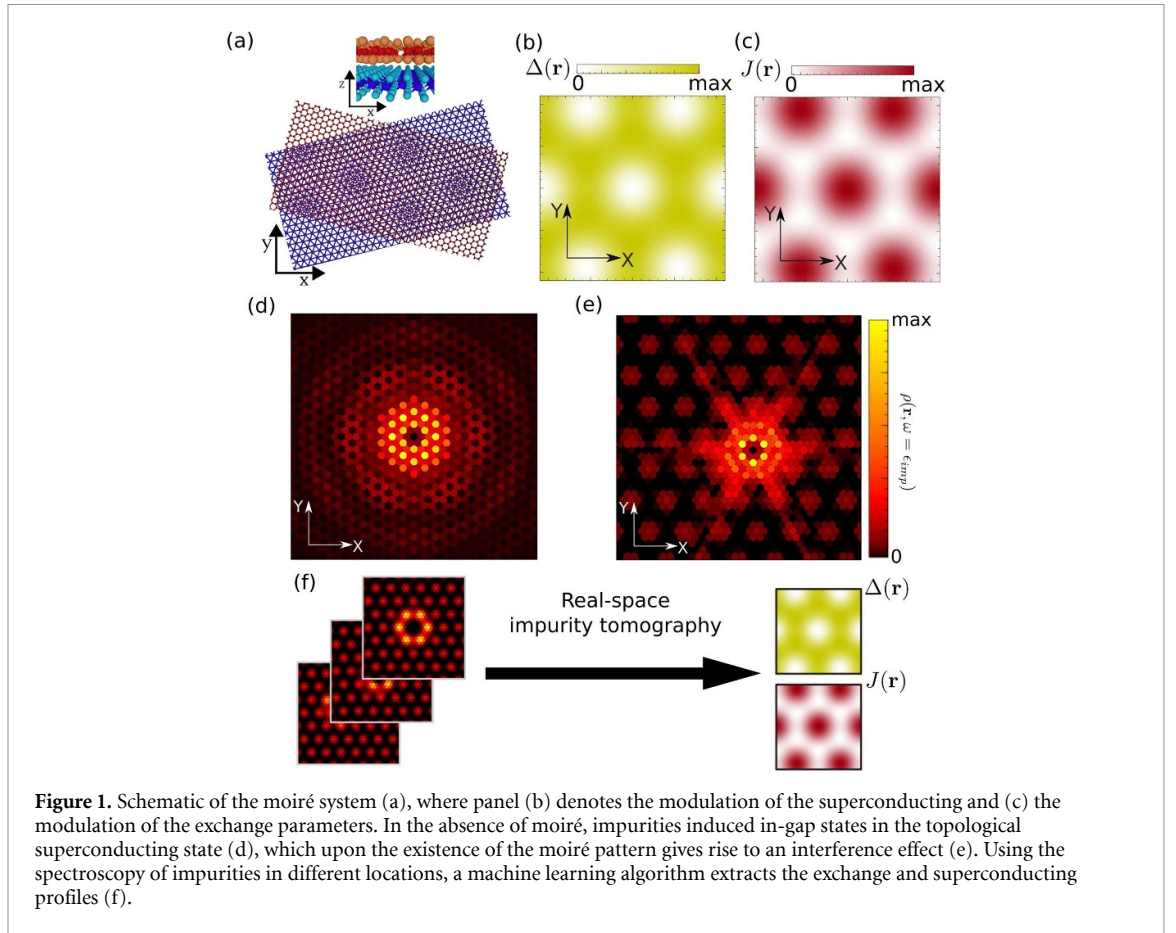
and the superconducting order by

$$\mathcal{H}_{\text{SC}} = \sum_i \Delta(\mathbf{r}) c_{i,\uparrow}^\dagger c_{i,\downarrow}^\dagger + h.c. \quad (3)$$

where  $J(\mathbf{r})$  and  $\Delta(\mathbf{r})$  parameterize the exchange coupling and induced s-wave superconductivity. The competition between the exchange field and the superconducting order leads to an induced modulated superconductivity stemming from the originally modulated exchange [72–74]. We take a modulation parametrized as  $f(\mathbf{r}) = c_0 + c_1 \sum_{n=1}^3 \cos(R^n \mathbf{q} \cdot \mathbf{r})$  where  $\mathbf{q}$  is the moiré superlattice wave vector, and  $R_n$  is the rotation matrix conserving  $C_3$  symmetry. The parameters  $c_0, c_1$  are defined so that  $\langle f(\mathbf{r}) \rangle = 0$ . The spatial profiles  $J(\mathbf{r})$  and  $\Delta(\mathbf{r})$  are written in terms of the previous spatial dependence as

$$\begin{aligned} J(\mathbf{r}) &= J_0 + \delta_J f(\mathbf{r}) \\ \Delta(\mathbf{r}) &= \Delta_0 + \delta_\Delta (1 - f(\mathbf{r})) \end{aligned} \quad (4)$$

$J_0$  and  $\Delta_0$  parametrize the average magnitude of the modulated exchange and superconducting profiles, whereas  $\delta_J$  and  $\delta_\Delta$  control the amplitude of the moiré modulation. For the sake of concreteness we take  $J_0 = \lambda_R$  and  $\Delta_0 = \lambda_R/2$ . The relative signs of  $f(\mathbf{r})$  in  $J(\mathbf{r})$  and  $\Delta(\mathbf{r})$  are taken so that when the superconducting order is maximum, the exchange is minimum (figures 1(b) and (c)).



Local non-magnetic impurities are included adding a potential scattering term of the form

$$\mathcal{H}_{\text{imp}} = W \sum_s c_{n,s}^\dagger c_{n,s} \quad (5)$$

where  $\mathcal{H}_{\text{imp}}$  defines the impurity Hamiltonian at site  $n$  with an on-site potential  $w$ . We focus on the strong impurity limit in which the site is effectively removed from the low energy manifold taking  $W = 100t$ . The full Hamiltonian of the defective system takes the form

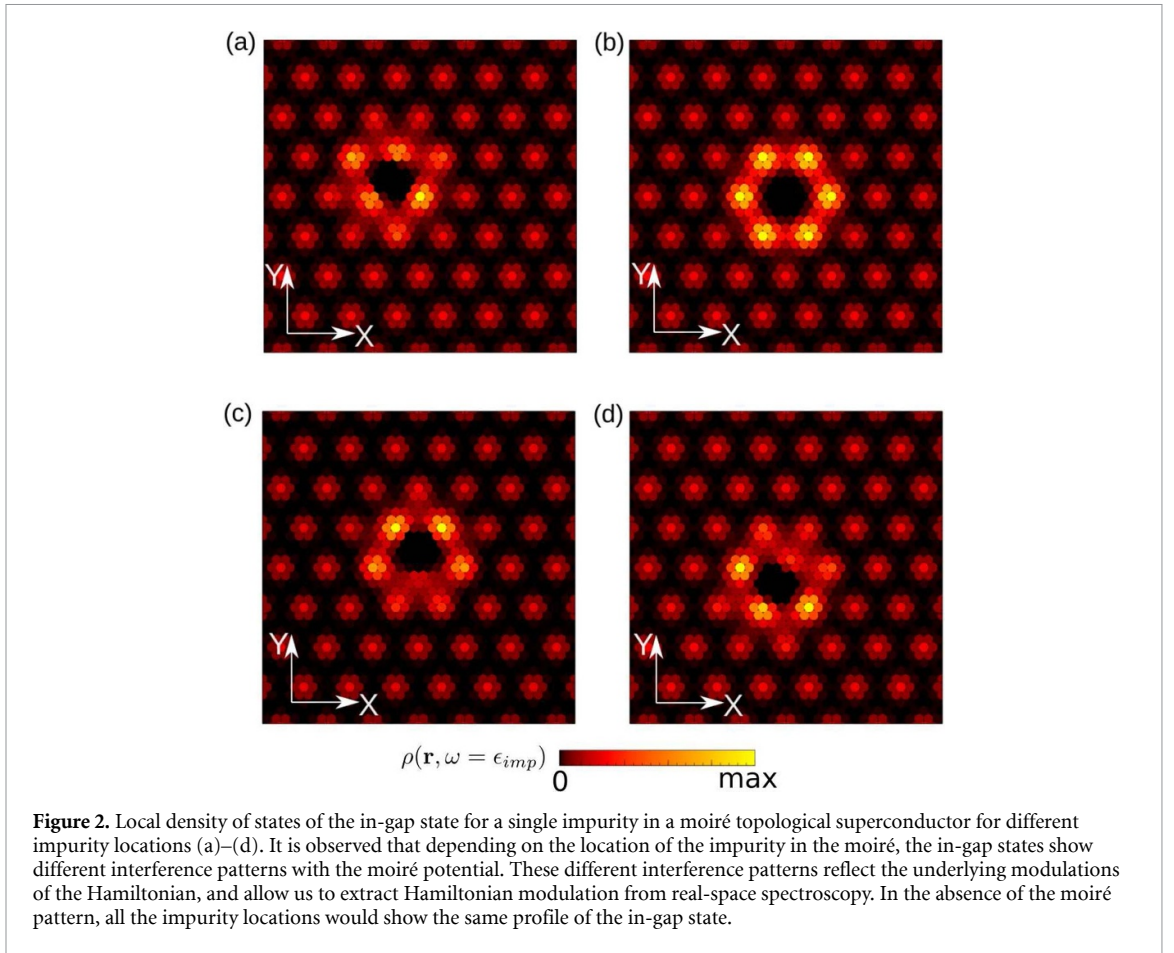
$$\mathcal{H} = \mathcal{H}_0 + \mathcal{H}_{\text{imp}} \quad (6)$$

The impurity gives rise to an in-gap state both in the absence (figure 1(d)) and presence (figure 1(e)) of a moiré modulation. It is important to note that, due to the presence of the moiré pattern, the impact of an impurity depends on its location with respect to the moiré modulation. Specifically, as shown in the LDOS of figure 2, the interference between the impurity state and the moiré potential gives rise to different patterns depending on the location. This interference fully disappears when  $\delta_J$  and  $\delta_\Delta$  are switched off. We will show that our machine learning algorithm will use the interference between the different locations of impurities to extract the values of the Hamiltonian modulations.

We finally elaborate on the computational procedure to solve this model in the limit of a single impurity in an otherwise pristine system. For this purpose, we will use Green's function embedding method [55, 75, 76]. The embedding method relies on extracting the Green's function from the Dyson equation of the defective system

$$G_V(\omega) = [\omega - H_V - \Sigma(\omega) + i0^+]^{-1} \quad (7)$$

where  $G_V(\omega)$  is the Green's function of the defective model,  $H_V$  the Hamiltonian of the defective unit cell, and  $\Sigma(\omega)$  the selfenergy induced by the pristine system. The selfenergy  $\Sigma(\omega)$  can be obtained from the Dyson equation for the pristine model  $\Sigma(\omega) = \omega - H_0 - G_0(\omega)^{-1} + i0^+$  with  $H_0$  the Hamiltonian of the



pristine unit cell, where we take the Bloch's representation of the pristine unit cell Green's function  $G_0(\omega) = \frac{1}{(2\pi)^2} \int [\omega - H_{\mathbf{k}} + i0^+]^{-1} d^2\mathbf{k}$  where  $H_{\mathbf{k}}$  is the Bloch's Hamiltonian.

The LDOS used as input for our algorithm is obtained as

$$\rho(\mathbf{r}, \omega) = -\frac{1}{\pi} \sum_{s, \tau} \langle \mathbf{r}, s, \tau | \text{Im}(G_V(\omega)) | \mathbf{r}, s, \tau \rangle \quad (8)$$

where  $s$  and  $\tau$  are the spin and Nambu indexes. The in-gap state  $\varepsilon_{imp}$  is located using an iterative algorithm in the energy window of the topological superconducting gap. From an experimental point of view, a finite noise of the spectroscopy will be present, and thus the robustness of our algorithm will be important with regards to its experimental implementation. We emulate the impact of noise in the real-space spectroscopy as

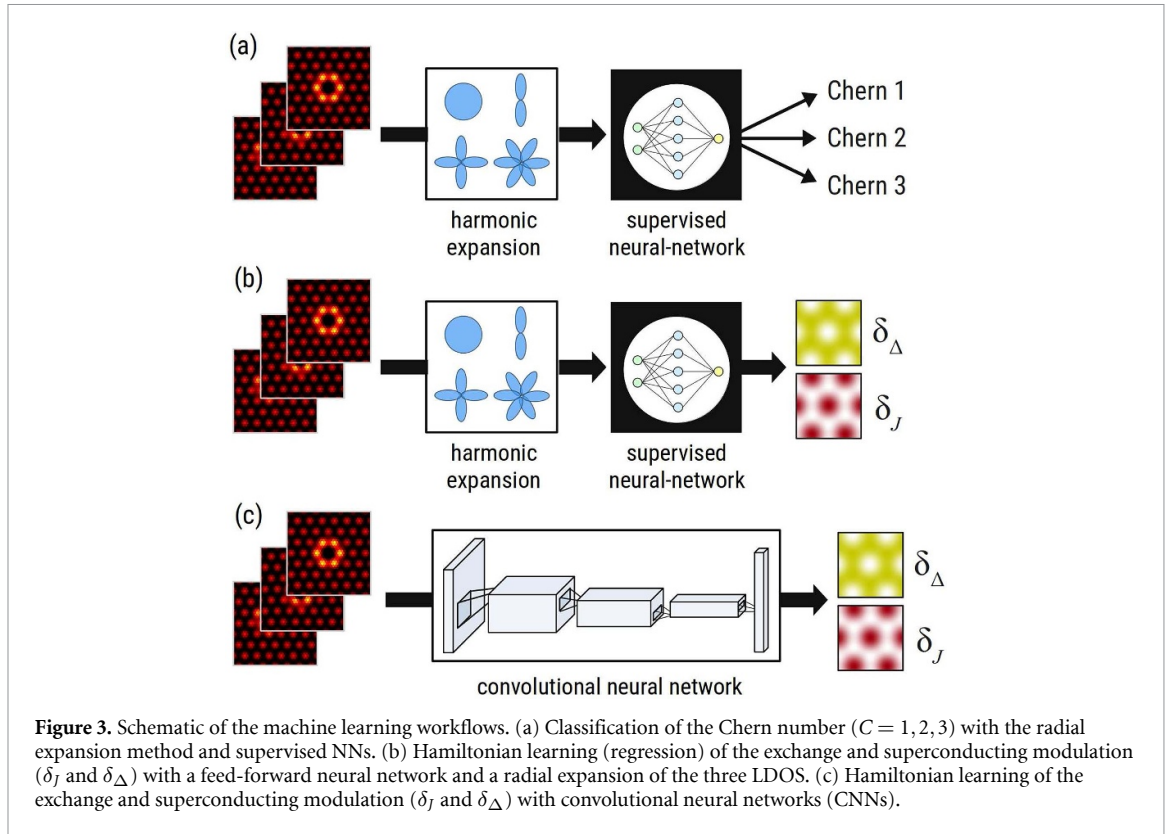
$$\rho_{noisy}(\mathbf{r}) = \rho(\mathbf{r}) + \chi(\mathbf{r}) \quad (9)$$

adding a noise background  $\chi(\mathbf{r}) = \chi_0 \cdot \mathcal{R}(\mathbf{r})$  to the LDOS  $\rho(\mathbf{r})$  where  $\chi_0$  is the noise magnitude and  $\mathcal{R}(\mathbf{r})$  is a random uniform noise distribution defined in the interval  $(-\langle \rho(\mathbf{r}) \rangle, \langle \rho(\mathbf{r}) \rangle)$  with  $\langle \rho(\mathbf{r}) \rangle$  as mean value of the LDOS.

## 2.2. Machine learning

The main idea of our real-space impurity tomography is to extract the underlying Hamiltonian by using the LDOS for different impurity positions as inputs as shown in figure 1(f). The extraction of the superconducting and exchange modulation is a non-trivial problem without a simple one-to-one correspondence to a single real-space spectroscopy.

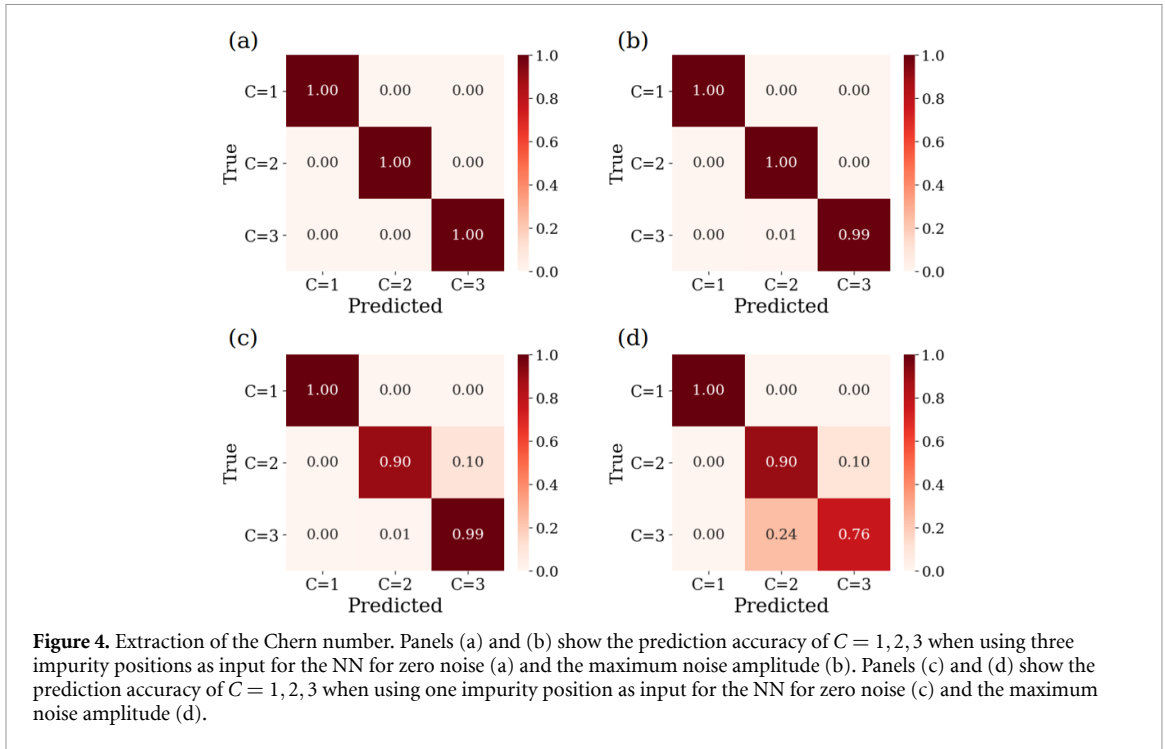
We will use a physics-inspired approach to compress the information contained in the LDOS with a harmonic expansion (see figures 3(a) and (b)). The coefficients of the power spectrum for each LDOS are then concatenated and fed into a fully-connected neural network (NN) as depicted in figure 3(b). The radial expansion works as follows. First, each individual LDOS is centered around the impurity position. Then, the harmonic expansion for the power spectrum is performed as



$$c_{ln} = \sum_{\alpha} \rho(\mathbf{r}_{\alpha}) e^{i\phi_{\alpha}} r_{\alpha}^n e^{-r_{\alpha}/\Lambda} \quad (10)$$

where  $c_{ln}$  are the coefficients of the expansion,  $\mathbf{r}_{\alpha} = r_{\alpha}(\cos \phi_{\alpha}, \sin \phi_{\alpha}, 0)$  the atomic sites taking as the origin the impurity site, and  $\Lambda$  is the typical localization length of the state [77]. In particular, we expand each LDOS into 24 complex  $c_{ln}$  coefficients, i.e. the input dimension of the NN is 144 after concatenating the real and imaginary components of the coefficients for three LDOS. We first train a fully-connected NN to perform classification of the Chern number of a given LDOS image which is compressed again into radial functions. The workflow is shown in figure 3(a). The NN architecture is shown in table 1. The loss function for this case is the *categorical crossentropy loss* and a *softmax-activation function* is used for the output layer. The training consists of 100 epochs, with a batch size of 16. The optimization is performed with the Adam optimizer and a learning rate of 0.001. Afterward, we create a supervised architecture to predict the Hamiltonian parameter of the exchange and superconducting modulation ( $\delta_J, \delta_\Delta$ ). For this regression task, the architecture of the NN is shown in table 2. We trained the NN for 100 epochs with a batch size of 16. For the optimization of the weights, we are using the stochastic gradient descent algorithm and the Adam optimizer [78] with a learning rate of 0.001. The loss function is the mean squared error (MSE). For the training and testing, we created LDOS for 2000 Hamiltonians for each Chern number where we varied the parameter  $\delta_J \in [0, 2\lambda_R]$  and  $\delta_\Delta \in [0, \lambda_R]$ . This results in 6000 samples which we divided into a training set of 5400 and a test set of 600 examples. Finally, we take as a benchmark of our procedure a convolutional NN (CNN) [79] architecture. We take an analogous workflow as shown in figure 3(c), where three LDOS with different impurity positions are fed into the CNN which predicts the modulation of the exchange or superconductivity as a regression task. The architecture of the CNN is shown in table 3, where three CNN networks are concatenated into a fully-connected NN and trained simultaneously with three input LDOS. For the training, we used 50 epochs with a batch size of 16.

It is finally worth noting that our machine learning approach allows us to exploit the spatial resolution of scanning tunneling microscopy. In the case of unconventional superconductors, the non-trivial interference between bound states provides information about the underlying electronic state, information that is often not accessible with other probes. Other approaches to Hamiltonian learning use the energy and entanglement spectra for Hamiltonian inference [80], or employing time-resolved measurements to extract Hamiltonian parameters [7]. However, performing those measurements for unconventional superconductors is greatly challenging, whereas the measurements of the LDOS in our impurity tomography approach are standard in scanning probe experiments in two-dimensional superconductors.



### 3. Results and discussion

#### 3.1. Chern number extraction

The first problem we tackle is to determine the Chern number from one or three LDOS with different impurity locations. The measurement of topological invariants in topological superconductors is a practical open challenge [81–86], as due to their topological nature, local order parameters cannot be defined for these states. The appearance of in-gap modes alone is not enough to assess the topological invariant of a superconductor, as in-gap states can appear in both trivial and topological superconductors [87]. Interestingly, the inclusion of a moiré pattern leads to subtle changes in the spatial distribution of in-gap states [55]. As we will show below, the fine structure of the in-gap modes allows for extracting the topological invariant of the underlying state.

In the following, we elaborate on the procedure to extract the topological invariant solely from the real-space spectroscopy images of single impurities. The input of the algorithm consists of the real-space spectroscopy for three impurity locations, and its output is the topological invariant. To extract the topological invariant, we trained a NN to perform the classification into the 3 non-trivial Chern numbers. The results are shown in figure 4 in the form of confusion matrices for three figures 4(a), (b) and one LDOS figures 4(c) and (d) as input. For one LDOS as input, we achieve an average accuracy of 96.3% for the test data with zero noise (c) and 88.7% with the maximum noise amplitude of  $\chi_0 = 0.4$ . The confusion matrix shows that  $C = 1$  can be predicted with 100% accuracy in both cases, the NN is only confused in the prediction between  $C = 2$  and  $C = 3$ . Taking three real-space spectroscopies with different impurity positions as input, we obtain a testing accuracy of 100% for zero noise (a) and 99.7% for the maximum noise amplitude. This highlights that combining three real-space spectroscopies for different impurity locations substantially increases the accuracy of the topological invariant predictions. These results show, that it is possible to extract the Chern number by just one LDOS with a random impurity position even in the case of very noisy data.

#### 3.2. Exchange field extraction

In the following, we show how the real-space impurity tomography allows extracting the values of the moiré Hamiltonian parameters. We start with the modulation of the exchange coupling, which is intuitively the parameter that will impact the real-space spectroscopy in the strongest way. This stems from the fact that the local exchange coupling creates in-gap Yu-Shiba-Rusinov modes inside the original superconducting gap  $\Delta$  [32, 34, 88–94], and these modes form the low energy electronic structure leading to a topological

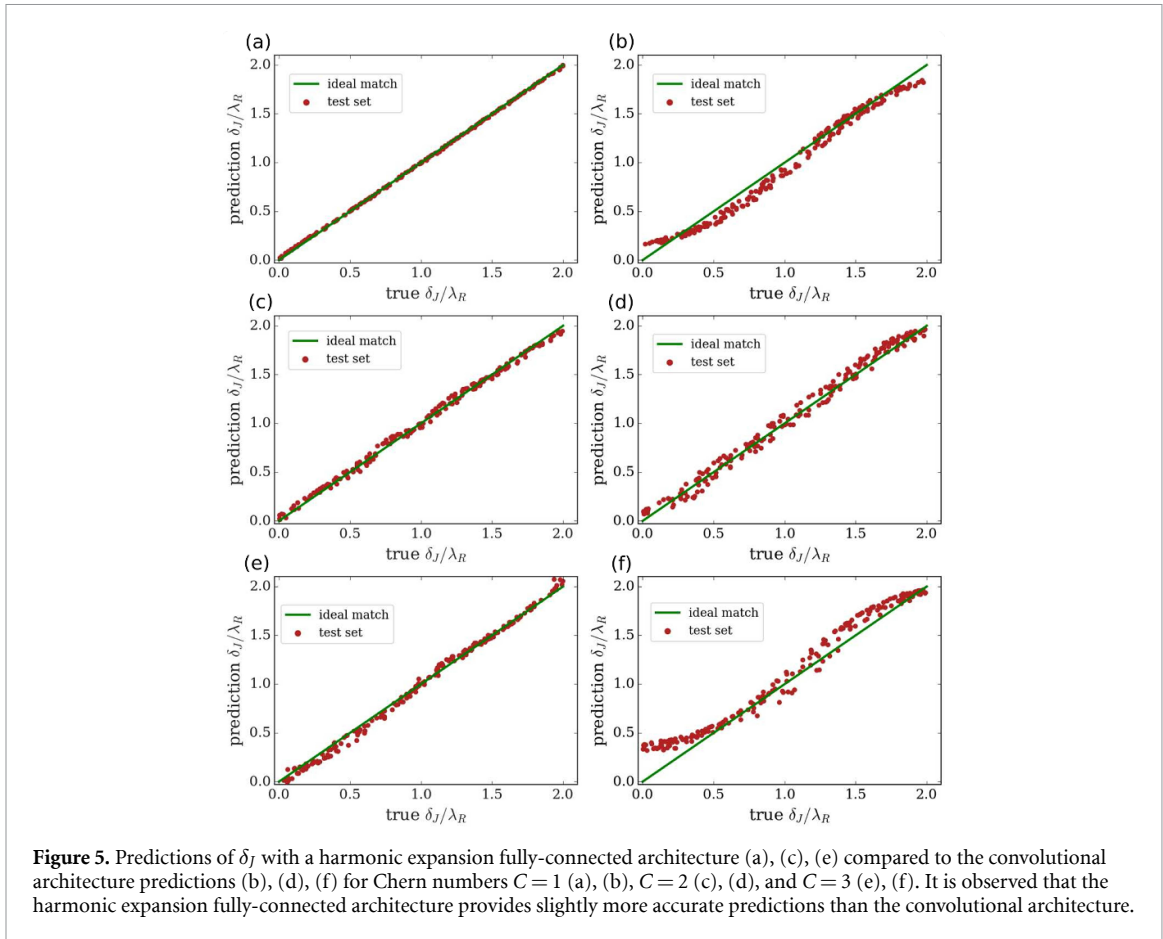


**Figure 5.** Predictions of  $\delta_J$  with a harmonic expansion fully-connected architecture (a), (c), (e) compared to the convolutional architecture predictions (b), (d), (f) for Chern numbers  $C = 1$  (a), (b),  $C = 2$  (c), (d), and  $C = 3$  (e), (f). It is observed that the harmonic expansion fully-connected architecture provides slightly more accurate predictions than the convolutional architecture.

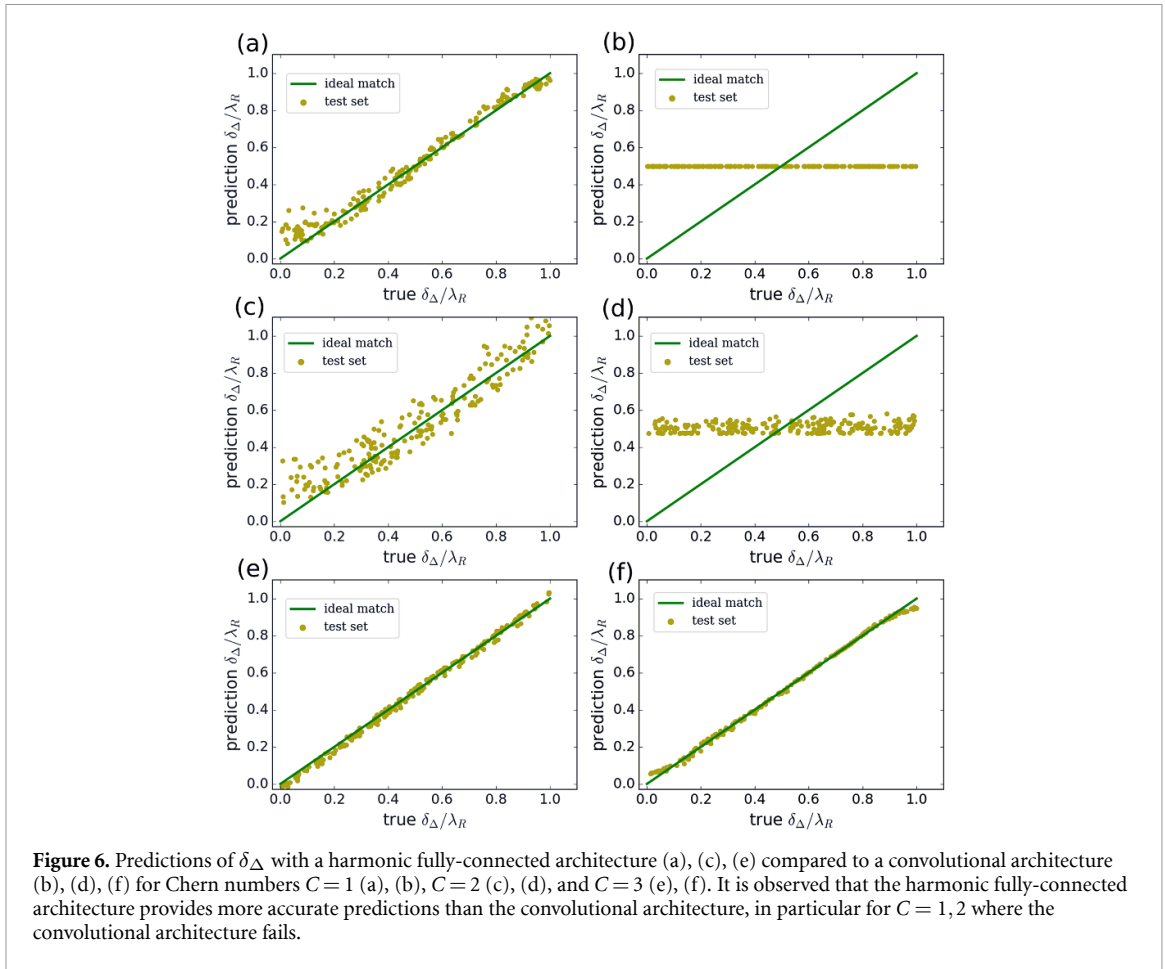
superconducting state. As a result, low energy bands reflect the periodicity of the exchange modulation, and their associated in-gap modes in the presence of impurities inherit the same dependence [34, 55].

We take as input the real-space spectroscopy for three impurity locations, leading as output the modulation strength of the exchange coupling in the system. We train different architectures for each Chern number, including CNNs of the full spectroscopy and the harmonic expansion of the impurity states. The results, shown in figure 5 demonstrate that real-space spectroscopy of the impurities allows extracting the modulation of the exchange coupling with both procedures. Specifically, it is shown that both convolutional and harmonic expansion obtain a substantial accuracy in the extraction, specifically leading to a typical error of  $\mathcal{E}[\delta_J] = 0.01$  for the convolutional algorithm and  $\mathcal{E}[\delta_J] = 0.0072$  for the harmonic expansion. We observe that the harmonic algorithm becomes slightly more accurate than the convolutional method. Interestingly, the difference between both methods becomes much more dramatic in the extraction of superconducting order values and modulations.

### 3.3. Superconducting order extraction

We now move to consider the extraction of the local superconducting order  $\Delta(\mathbf{r})$  with real-space impurity tomography. It is interesting to note that the impact of modulation of  $\Delta$  in the low energy states is expected to be more subtle than the exchange. While the energy location of a Yu-Shiba-Rusinov strongly depends on  $J$ , the value of the superconducting gap only leads to proportional renormalization of the energy [87].

We show in figure 6 the extraction of the superconducting modulation using the harmonic expansion with supervised learning (figures 6(a), (c) and (e)) and the CNN architecture (figures 6(b), (d) and (f)), for  $C = 1$  (figures 6(a) and (b)),  $C = 2$  (figures 6(c) and (d)) and  $C = 3$  (figures 6(e) and (f)). In the case  $C = 3$  (figures 6(e) and (f)), we observe that both architectures are capable of predicting the superconducting modulation. Interestingly, for  $C = 1$  (figures 6(a) and (b)) and  $C = 2$  (figures 6(c) and (d)), the convolutional architecture is incapable of predicting correct superconducting modulations, whereas the fully-connected harmonic expansion successfully predicts it. Typical errors of the NNs are  $\mathcal{E}[\delta_\Delta] = 0.30, 0.29, 0.008$  for  $C = 1, 2, 3$  for CNN and  $\mathcal{E}[\delta_\Delta] = 0.03, 0.024, 0.008$  for  $C = 1, 2, 3$  for harmonic expansion with the fully-connected NN. This phenomenology should be contrasted with the exchange modulation, where both architectures showed similar performance. The success of the fully-connected harmonic expansion and the



failure of the CNN architecture demonstrate that the extraction of superconducting modulations represents a much more challenging problem than the exchange modulation. In particular, our harmonic expansion shows that such a physically-motivated procedure allows extracting Hamiltonian parameters stemming from highly subtle changes in the real-space spectroscopy.

### 3.4. Noisy Hamiltonian extraction

In the following, we address the extraction of the Hamiltonian in the presence of noisy data. For the sake of concreteness, we focus on the harmonic fully-connected architecture, as the superconducting modulation can be predicted with that one. We show in figure 7 the evolution of the correlation between predictions and true values as a function of increasing noise. We define prediction fidelity as

$$\mathcal{F}(\delta^{\text{pred}}, \delta^{\text{true}}) = \frac{|\langle \delta^{\text{pred}} \delta^{\text{true}} \rangle - \langle \delta^{\text{true}} \rangle \langle \delta^{\text{pred}} \rangle|}{\sqrt{(\langle (\delta^{\text{true}})^2 \rangle - \langle \delta^{\text{true}} \rangle^2) (\langle (\delta^{\text{pred}})^2 \rangle - \langle \delta^{\text{pred}} \rangle^2)}} \quad (11)$$

is defined in the interval  $\mathcal{F} \in [0, 1]$ , where  $\mathcal{F} = 1$  corresponds to the best prediction accuracy  $\delta^{\text{pred}} = \delta^{\text{true}}$  and  $\mathcal{F} = 0$  corresponds to no predictive accuracy. Focusing first on the exchange modulation shown in figure 7, we observe that even substantial noise allows to infer the value of its modulation for the Chern numbers. The robustness of the exchange modulation extraction is consistent with the fact that the NN architecture was capable of providing faithful predictions of the parameter. This resilience to noise stems from the strong dependence of the Yu–Shiba–Rusinov states on the local exchange, which directly impacts the real-space profile of the spectroscopy. The prediction of the superconducting modulation represents however a bigger challenge as shown in figure 7. In the cases  $C = 1, 2$  (figures 7(a)–(d)), the most challenging ones, we observe that magnitudes of noise around  $\chi_0 = 0.005$  break down the predictions. In stark contrast, systems with  $C = 3$  are resilient to levels of noise magnitudes up to  $\chi_0 = 0.2$  as shown in figures 7(e) and (f). The difference in the robustness between  $C = 1, 2$  and  $C = 3$  can be rationalized by recalling that the CNN architecture is not capable of providing predictions for  $C = 1, 2$ , but it gave reliable predictions for  $C = 3$ . Interestingly, despite the superconducting modulation creating a very subtle impact in the real-space

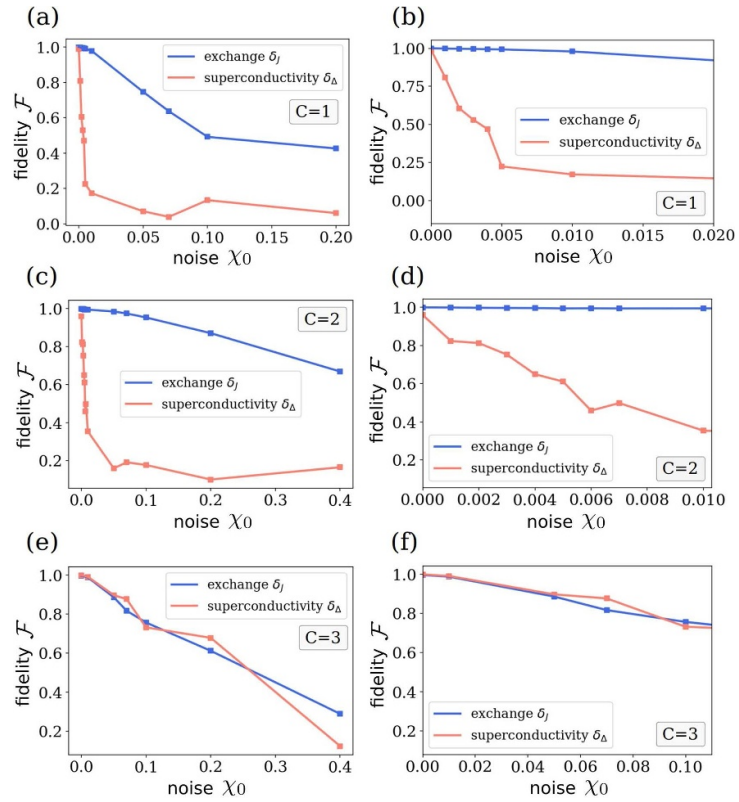


**Figure 7.** Analysis of the correlation between the predicted and real values of the exchange and superconducting modulation as a function of the noise level for  $C = 1$  (a), (b),  $C = 2$  (c), (d), and  $C = 3$  (e), (f). Panels (a), (c), (e) correspond to a larger noise range, whereas (b), (d), (f) correspond to the low noise limit. It is observed that exchange modulations  $\delta_j$  are more resilient to noise than superconducting modulation predictions  $\delta_\Delta$ .

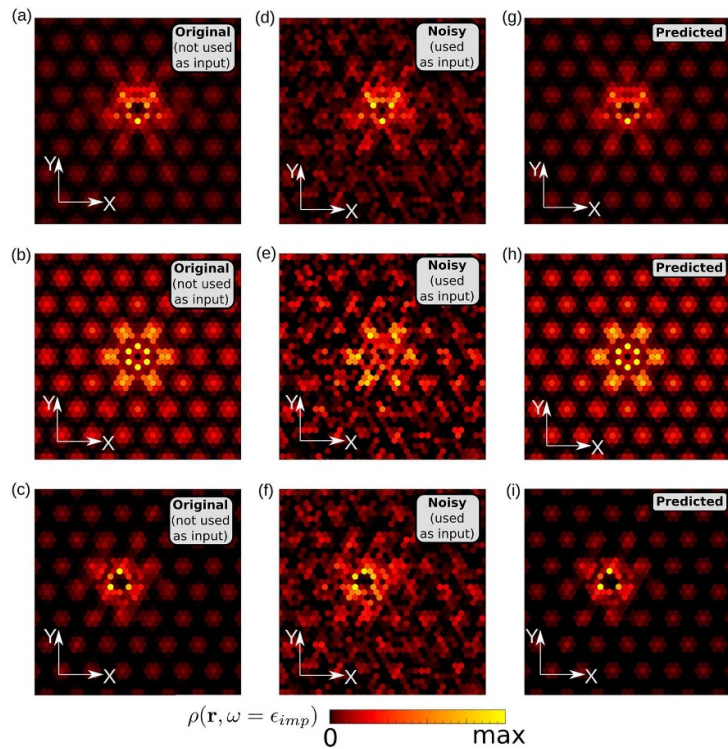


**Figure 8.** Local density of states of the in-gap state for a single impurity in a moiré superlattice with  $C = 3$  for three different locations for (a)–(c). Panels (d)–(f) show the real-space spectroscopy with  $\chi_0 = 0.2$  noise amplitude, which is used as input for the machine learning algorithm. Panels (g)–(i) show the real-space spectroscopy associated to the predicted Hamiltonian by the neural network.

spectroscopy, our algorithm is capable of extracting the modulation amplitude from noisy data for different Chern numbers. Finally, we show in figure 8(a) comparison between the spectroscopies for the pristine data (figures 8(a)–(c)), the noisy data provided as input to our algorithm (figures 8(d)–(f)) and the spectroscopy computed with the parameters predicted by the Hamiltonian extraction (figures 8(g)–(i)). It is observed that the spectroscopy predictions are nearly indistinguishable from the original ones, showing that our algorithm is capable of solving the inverse problem of inferring the Hamiltonian from the spectroscopy.

## 4. Conclusions

To summarize, we have shown that interference effects of in-gap states allow extracting Hamiltonian moiré parameters and topological invariants in an artificial topological superconductor from real-space spectroscopy patterns. Our approach is based on a supervised learning procedure that exploits the patterns obtained in in-gap states for different impurity locations simultaneously. We showed that our technique can be readily implemented with a convolution NN architecture that combines several impurity locations simultaneously. Furthermore, we showed that by leveraging an orbital expansion of the impurity modes, a more robust machine-learning approach can be developed. Specifically, our procedure using a harmonic expansion is capable of extracting both parameter values and their modulations even in the presence of noise. We demonstrate that the combination of different locations dramatically increases the accuracy of Hamiltonian parameter inference, exemplifying how parameter inference benefits from features that our algorithm extracts from several impurity locations. Our results establish a machine learning methodology that exploits local impurity engineering to extract non-trivial parameters in artificial topological systems. Our demonstration exploits data directly accessible in scanning tunneling microscopy experiments and is robust in the presence of noise, establishing a realistic method to extract Hamiltonian parameters from readily accessible experimental data in complex quantum materials.

## Data availability statement

All data that support the findings of this study are included within the article (and any supplementary files).

## Acknowledgments

We acknowledge the computational resources provided by the Aalto Science-IT project, and the financial support from the Academy of Finland Projects Nos. 331342, 336243 and 358088, the Jane and Aatos Erkko Foundation. We thank P Liljeroth, S Kezilebieke and T Ojanen for useful discussions.

## Appendix. Network architectures

**Table 1.** Architecture of the fully-connected NN of the expansion method. Used for the classification of the Chern number.

fully-connected NN (classification)	
Layer	Output shape
<b>Harmonic expansion</b>	
InputLayer	(48 · 3) <i>Preprocessing</i>
Dense	(200) <i>48 params / LDOS</i>
Dropout	(200)
Dense	(100)
Dropout	(100)
Dense	(20)
Dropout	(20)
Dense	(3)
Total parameters	51 183

**Table 2.** Architecture of the fully-connected NN of the expansion method. Used for the regression of the Hamiltonian parameters.

fully-connected NN (regression)	
Layer	Output shape
<b>Harmonic expansion</b>	
InputLayer	(48 · 3) <i>Preprocessing</i>
Dense	(300) <i>48 params / LDOS</i>
Dropout	(300)
Dense	(2)
Total parameters	15 302

**Table 3.** Architecture of the CNN. Used for the regression of the Hamiltonian parameters.

CNN	
Layer	Output shape
<b>Combine three CNNs:</b>	
InputLayer	(55, 55, 1)
Conv2D	(55, 55, 32)
MaxPooling2D	(27, 27, 32)
Conv2D	(27, 27, 64)
MaxPooling2D	(13, 13, 64)
Flatten	(10 816)
<b>Fully-connected NN</b>	
Concatenate	(32 448) <i>combine 3 CNNs</i>
Dense	(200)
Dense	(50)
Dense	(1) or (2)
Total parameters	6556 349

## ORCID iDs

Maryam Khosravian  <https://orcid.org/0000-0002-2760-108X>

Rouven Koch  <https://orcid.org/0000-0002-8917-3631>

Jose L Lado  <https://orcid.org/0000-0002-9916-1589>

## References

- [1] Garrison J R and Grover T 2018 Does a single eigenstate encode the full Hamiltonian? *Phys. Rev. X* **8** 021026
- [2] Chertkov E and Clark B K 2018 Computational inverse method for constructing spaces of quantum models from wave functions *Phys. Rev. X* **8** 031029

- [3] Turkeshi X, Mendes-Santos T, Giudici G and Dalmonte M 2019 Entanglement-guided search for parent Hamiltonians *Phys. Rev. Lett.* **122** 150606
- [4] Koch R and Lado J L 2022 Designing quantum many-body matter with conditional generative adversarial networks *Phys. Rev. Res.* **4** 033223
- [5] Valenti A, van Nieuwenburg E, Huber S and Greplova E 2019 Hamiltonian learning for quantum error correction *Phys. Rev. Res.* **1** 033092
- [6] Karjalainen N, Lippo Z, Chen G, Koch R, Fumega A O and Lado J L 2023 Hamiltonian inference from dynamical excitations in confined quantum magnets *Phys. Rev. Appl.* **20** 024054
- [7] Che L, Wei C, Huang Y, Zhao D, Xue S, Nie X, Li J, Lu D and Xin T 2021 Learning quantum Hamiltonians from single-qubit measurements *Phys. Rev. Res.* **3** 023246
- [8] Yang K, Phark S-H, Bae Y, Esat T, Willke P, Ardavan A, Heinrich A J and Lutz C P 2021 Probing resonating valence bond states in artificial quantum magnets *Nat. Commun.* **12** 993
- [9] Bryant B, Spinelli A, Wagenaar J J T, Gerrits M and Otte A F 2013 Local control of single atom magnetocrystalline anisotropy *Phys. Rev. Lett.* **111** 127203
- [10] Yan S, Choi D-J, Burgess J A J, Rolf-Pissarczyk S and Loth S 2015 Three-dimensional mapping of single-atom magnetic anisotropy *Nano Lett.* **15** 1938–42
- [11] Li Z, Zou L and Hsieh T H 2020 Hamiltonian tomography via quantum quench *Phys. Rev. Lett.* **124** 160502
- [12] Bairey E, Arad I and Lindner N H 2019 Learning a local Hamiltonian from local measurements *Phys. Rev. Lett.* **122** 020504
- [13] Huang H-Y, Tong Y, Fang Di and Su Y 2023 Learning many-body Hamiltonians with Heisenberg-limited scaling *Phys. Rev. Lett.* **130** 200403
- [14] Valenti A, Jin G, Léonard J, Huber S D and Greplova E 2022 Scalable Hamiltonian learning for large-scale out-of-equilibrium quantum dynamics *Phys. Rev. A* **105** 023302
- [15] Kokail C, van Bijnen R, Elben A, Vermersch Bit and Zoller P 2021 Entanglement Hamiltonian tomography in quantum simulation *Nat. Phys.* **17** 936–42
- [16] Gentile A A, Flynn B, Knauer S, Wiebe N, Paesani S, Granade C E, Rarity J G, Santagati R and Laing A 2021 Learning models of quantum systems from experiments *Nat. Phys.* **17** 837–43
- [17] Di Franco C, Paternostro M and Kim M S 2009 Hamiltonian tomography in an access-limited setting without state initialization *Phys. Rev. Lett.* **102** 187203
- [18] Carrasquilla J 2020 Machine learning for quantum matter *Adv. Phys. X* **5** 1797528
- [19] Schirmer S G and Oi D K L 2009 Two-qubit Hamiltonian tomography by Bayesian analysis of noisy data *Phys. Rev. A* **80** 022333
- [20] Seveso L and Paris M G A 2018 Estimation of general Hamiltonian parameters via controlled energy measurements *Phys. Rev. A* **98** 032114
- [21] Hincks I, Granade C and Cory D G 2018 Statistical inference with quantum measurements: methodologies for nitrogen vacancy centers in diamond *New J. Phys.* **20** 013022
- [22] Wang J et al 2017 Experimental quantum Hamiltonian learning *Nat. Phys.* **13** 551–5
- [23] Gebhart V, Santagati R, Gentile A A, Gauger E M, Craig D, Ares N, Banchi L, Marquardt F, Pezzè L and Bonato C 2023 Learning quantum systems *Nat. Rev. Phys.* **5** 141–56
- [24] Koch R, van Driel D, Bordin A, Lado J L and Greplova E 2023 Adversarial Hamiltonian learning of quantum dots in a minimal Kitaev chain (arXiv:2304.10852 [cond-mat.mes-hall])
- [25] Aikebaier F, Ojanen T and Lado J L 2023 Extracting electronic many-body correlations from local measurements with artificial neural networks *SciPost Phys. Core* **6** 030
- [26] Aikebaier F, Ojanen T and Lado J L 2023 Machine learning the Kondo entanglement cloud from local measurements (arXiv:2311.07253 [cond-mat.str-el])
- [27] Fiderer L J, Schuff J and Braun D 2021 Neural-network heuristics for adaptive bayesian quantum estimation *PRX Quantum* **2** 020303
- [28] Sobral Jão A, Obernauer S, Turkel S, Pasupathy A N and Scheurer M S 2023 Machine learning the microscopic form of nematic order in twisted double-bilayer graphene *Nat. Commun.* **14** 5012
- [29] Andrei E Y, Efetov D K, Jarillo-Herrero P, MacDonald A H, Mak K F, Senthil T, Tutuc E, Yazdani A and Young A F 2021 The marvels of moiré materials *Nat. Rev. Mater.* **6** 201–6
- [30] Gibertini M, Koperski M, Morpurgo A F and Novoselov K S 2019 Magnetic 2D materials and heterostructures *Nat. Nanotechnol.* **14** 408–19
- [31] Liu Y, Weiss N O, Duan X, Cheng H-C, Huang Y and Duan X 2016 Van der waals heterostructures and devices *Nat. Rev. Mater.* **1** 16042
- [32] Kezilebieke S, Huda M N, Vaño V, M, Ganguli S C, Silveira O J, Glodzik S, Foster A S, Ojanen T and Liljeroth P 2020 Topological superconductivity in a van der waals heterostructure *Nature* **588** 424–8
- [33] Kezilebieke S et al 2021 Electronic and magnetic characterization of epitaxial CrBr<sub>3</sub> monolayers on a superconducting substrate *Adv. Mater.* **33** 2006850
- [34] Kezilebieke S, Vaño V, Huda M N, Aapro M, Ganguli S C, Liljeroth P and Lado J L 2022 Moiré-enabled topological superconductivity *Nano Lett.* **22** 328–33
- [35] Persky E, Bjørliig A V, Feldman I, Almoalem A, Altman E, Berg E, Kimchi I, Ruhman J, Kanigel A and Kalisky B 2022 Magnetic memory and spontaneous vortices in a van der Waals superconductor *Nature* **607** 692–6
- [36] Ai L et al 2021 Van der waals ferromagnetic Josephson junctions *Nat. Commun.* **12** 6580
- [37] Lopes dos Santos J M B, Peres N M R and Castro Neto A H 2007 Graphene bilayer with a twist: electronic structure *Phys. Rev. Lett.* **99** 256802
- [38] Suárez Morell E, Correa J D, Vargas P, Pacheco M and Barticevic Z 2010 Flat bands in slightly twisted bilayer graphene: tight-binding calculations *Phys. Rev. B* **82** 121407
- [39] Bistritzer R and MacDonald A H 2011 Moire bands in twisted double-layer graphene *Proc. Natl Acad. Sci.* **108** 12233–7
- [40] Fang S and Kaxiras E 2016 Electronic structure theory of weakly interacting bilayers *Phys. Rev. B* **93** 235153
- [41] Sboychakov A O, Rakhmanov A L, Rozhkov A V and Nori F 2015 Electronic spectrum of twisted bilayer graphene *Phys. Rev. B* **92** 075402
- [42] Cao Y et al 2018 Correlated insulator behaviour at half-filling in magic-angle graphene superlattices *Nature* **556** 80–84
- [43] Cao Y, Fatemi V, Fang S, Watanabe K, Taniguchi T, Kaxiras E and Jarillo-Herrero P 2018 Unconventional superconductivity in magic-angle graphene superlattices *Nature* **556** 43–50

- [44] Yankowitz M, Chen S, Polshyn H, Zhang Y, Watanabe K, Taniguchi T, Graf D, Young A F and Dean C R 2019 Tuning superconductivity in twisted bilayer graphene *Science* **363** 1059–64
- [45] Lu X et al 2019 Superconductors, orbital magnets and correlated states in magic-angle bilayer graphene *Nature* **574** 653–7
- [46] Chen G et al 2019 Signatures of tunable superconductivity in a trilayer graphene moiré superlattice *Nature* **572** 215–9
- [47] Arora H S et al 2020 Superconductivity in metallic twisted bilayer graphene stabilized by WSe<sub>2</sub> *Nature* **583** 379–84
- [48] Cao Y, Park J M, Watanabe K, Taniguchi T and Jarillo-Herrero P 2021 Pauli-limit violation and re-entrant superconductivity in moiré graphene *Nature* **595** 526–31
- [49] Sharpe A L, Fox E J, Barnard A W, Finney J, Watanabe K, Taniguchi T, Kastner M A and Goldhaber-Gordon D 2019 Emergent ferromagnetism near three-quarters filling in twisted bilayer graphene *Science* **365** 605
- [50] Xie Y et al 2021 Fractional chern insulators in magic-angle twisted bilayer graphene *Nature* **600** 439–43
- [51] Wong D, Nuckolls K P, Oh M, Lian B, Xie Y, Jeon S, Watanabe K, Taniguchi T, Bernevig B A and Yazdani A 2020 Cascade of electronic transitions in magic-angle twisted bilayer graphene *Nature* **582** 198–202
- [52] Zondiner U et al 2020 Cascade of phase transitions and Dirac revivals in magic-angle graphene *Nature* **582** 203–8
- [53] Saito Y, Yang F, Ge J, Liu X, Taniguchi T, Watanabe K, Li J I A, Berg E and Young A F 2021 Isospin Pomeranchuk effect in twisted bilayer graphene *Nature* **592** 220–4
- [54] Datta A, Calderón M J, Camjayi A and Bascones E 2023 Heavy quasiparticles and cascades without symmetry breaking in twisted bilayer graphene (arXiv:2301.13024)
- [55] Khosravian M and Lado J L 2022 Impurity-induced excitations in a topological two-dimensional ferromagnet/superconductor van der waals moiré heterostructure *Phys. Rev. Mater.* **6** 094010
- [56] Sufyan Ramzan M, Goodwin Z A H, Mostofi A A, Kuc A and Lischner J 2022 Effect of Coulomb impurities on the electronic structure of magic angle twisted bilayer graphene (arXiv:2211.01038 [cond-mat.mtrl-sci])
- [57] Lopez-Bezanilla A and Lado J L 2019 Defect-induced magnetism and Yu-Shiba-Rusinov states in twisted bilayer graphene *Phys. Rev. Mater.* **3** 084003
- [58] Ramirez A and Lado J L 2019 Impurity-induced triple point fermions in twisted bilayer graphene *Phys. Rev. B* **99** 245118
- [59] Baldo L, Löthman T, Holmval P and Black-Schaffer A M 2023 Defect-induced band restructuring and length scales in twisted bilayer graphene (arXiv:2304.03018 [cond-mat.mes-hall])
- [60] Naimer T, Zollner K, Gmitra M and Fabian J 2021 Twist-angle dependent proximity induced spin-orbit coupling in graphene/transition metal dichalcogenide heterostructures *Phys. Rev. B* **104** 195156
- [61] Zollner K and Fabian J 2021 Bilayer graphene encapsulated within monolayers of Ws<sub>2</sub> or Cr<sub>2</sub>Ge<sub>2</sub>Te<sub>6</sub>: tunable proximity spin-orbit or exchange coupling *Phys. Rev. B* **104** 075126
- [62] Högl P, Frank T, Zollner K, Kochan D, Gmitra M and Fabian J 2020 Quantum anomalous hall effects in graphene from proximity-induced uniform and staggered spin-orbit and exchange coupling *Phys. Rev. Lett.* **124** 136403
- [63] Hu X, Mao N, Wang H, Dai Y, Huang B and Niu C 2021 Quantum spin Hall effect in antiferromagnetic topological heterobilayers *Phys. Rev. B* **103** 085109
- [64] Karpik B et al 2019 Magnetic proximity in a van der Waals heterostructure of magnetic insulator and graphene *2D Mater.* **7** 015026
- [65] Beenakker C W J 2013 Search for Majorana fermions in superconductors *Annu. Rev. Condens. Matter Phys.* **4** 113–36
- [66] Alicea J 2012 New directions in the pursuit of Majorana fermions in solid state systems *Rep. Prog. Phys.* **75** 076501
- [67] Li J, Neupert T, Wang Z, MacDonald A H, Yazdani A and Bernevig B A 2016 Two-dimensional chiral topological superconductivity in Shiba lattices *Nat. Commun.* **7** 12297
- [68] Röntynen J and Ojanen T 2015 Topological superconductivity and high chern numbers in 2D ferromagnetic Shiba lattices *Phys. Rev. Lett.* **114** 236803
- [69] Ménard G C, Guissart S, Brun C, Leriche R T, Trif M, Debontridder F, Demaille D, Roditchev D, Simon P and Cren T 2017 Two-dimensional topological superconductivity in Pb/Co/Si(111) *Nat. Commun.* **8** 2040
- [70] Pöyhönen K, Sahlberg I, Westström A and Ojanen T 2018 Amorphous topological superconductivity in a Shiba glass *Nat. Commun.* **9** 2103
- [71] We take  $\lambda_R = 0.2t$  for all calculations
- [72] Gennes P G D 2018 *Superconductivity of Metals and Alloys* (CRC Press)
- [73] Kachin V, Ojanen T, Lado J L and Hyart T 2023 Effects of electron-electron interactions in the Yu-Shiba-Rusinov lattice model *Phys. Rev. B* **107** 174522
- [74] Buzdin A I 2005 Proximity effects in superconductor-ferromagnet heterostructures *Rev. Mod. Phys.* **77** 935–76
- [75] Lado J L and Fernández-Rossier J 2016 Unconventional Yu-Shiba-Rusinov states in hydrogenated graphene *2D Mater.* **3** 025001
- [76] Chen G and Lado J L 2020 Impurity-induced resonant spinon zero modes in Dirac quantum spin liquids *Phys. Rev. Res.* **2** 033466
- [77] We take  $\Lambda = 4a$ , with  $a$  the lattice constant in our calculations
- [78] Kingma D P and Ba J 2014 Adam: a method for stochastic optimization (arXiv:1412.6980 [cs.LG])
- [79] LeCun Y, Bengio Y and Hinton G 2015 Deep learning *Nature* **521** 436–44
- [80] Fujita H, Nakagawa Y O, Sugiura S and Oshikawa M 2018 Construction of Hamiltonians by supervised learning of energy and entanglement spectra *Phys. Rev. B* **97** 075114
- [81] Carvalho D, García-Martínez N A, Lado J L and Fernández-Rossier J 2018 Real-space mapping of topological invariants using artificial neural networks *Phys. Rev. B* **97** 115453
- [82] Rodríguez-Nieva J F and Scheurer M S 2019 Identifying topological order through unsupervised machine learning *Nat. Phys.* **15** 790–5
- [83] Scheurer M S and Slager R-J 2020 Unsupervised machine learning and band topology *Phys. Rev. Lett.* **124** 226401
- [84] Holanda N L and Griffith M A R 2020 Machine learning topological phases in real space *Phys. Rev. B* **102** 054107
- [85] Käming N, Dawid A, Kottmann K, Lewenstein M, Sengstock K, Dauphin A and Weitenberg C 2021 Unsupervised machine learning of topological phase transitions from experimental data *Mach. Learn.: Sci. Technol.* **2** 035037
- [86] Cao M D, Caccin M, Baireuther P, Hyart T and Fruchart M 2019 Machine learning assisted measurement of local topological invariants (arXiv:1901.03346 [cond-mat.dis-nn])
- [87] Balatsky A V, Vekhter I and Zhu J-X 2006 Impurity-induced states in conventional and unconventional superconductors *Rev. Mod. Phys.* **78** 373–433
- [88] Ruby M, Pientka F, Peng Y, von Oppen F, Heinrich B W and Franke K J 2015 End states and subgap structure in proximity-coupled chains of magnetic adatoms *Phys. Rev. Lett.* **115** 197204
- [89] Kim H, Palacio-Morales A, Posske T, Rózsa L, Palotás K, Szunyogh L, Thorwart M and Wiesendanger R 2018 Toward tailoring Majorana bound states in artificially constructed magnetic atom chains on elemental superconductors *Sci. Adv.* **4** eaar5251

- [90] Feldman B E, Randeria M T, Li J, Jeon S, Xie Y, Wang Z, Drozdov I K, Bernevig B A and Yazdani A 2016 High-resolution studies of the Majorana atomic chain platform *Nat. Phys.* **13** 286–91
- [91] Farinacci L, Ahmadi G, Reecht G, Ruby M, Bogdanoff N, Peters O, Heinrich B W, von Oppen F and Franke K J 2018 Tuning the coupling of an individual magnetic impurity to a superconductor: quantum phase transition and transport *Phys. Rev. Lett.* **121** 196803
- [92] Schneider L, Beck P, Posske T, Crawford D, Mascot E, Rachel S, Wiesendanger R and Wiebe J 2021 Topological Shiba bands in artificial spin chains on superconductors *Nat. Phys.* **17** 943–8
- [93] Theiler A, Björnson K and Black-Schaffer A M 2019 Majorana bound state localization and energy oscillations for magnetic impurity chains on conventional superconductors *Phys. Rev. B* **100** 214504
- [94] Mashkooi M, Pradhan S, Björnson K, Fransson J and Black-Schaffer A M 2020 Identification of topological superconductivity in magnetic impurity systems using bulk spin polarization *Phys. Rev. B* **102** 104501